Digital Twin Calibrated from Phaseless 28 GHz Measurement Scans for Indoor Exposure Assessment

Robin Wydaeghe, *Student Member, IEEE,* Olivier Caytan, *Member, IEEE,* Günter Vermeeren, Hendrik Rogier, *Senior Member, IEEE,* Sam Lemey, *Senior Member, IEEE,* Emmeric Tanghe, *Senior Member, IEEE,* and Wout Joseph, *Senior Member, IEEE*

***Abstract*—Absorbed power density is an important dosimetric quantity above 6 GHz under the 2020 International Commission on Non-Ionizing Radiation Protection (ICNIRP) guidelines. Its assessment in a real indoor environment requires spatial field distributions. Measurements are sparse and phaseless, while simulations require validation against measurements. We calibrate a ray-tracing digital twin of a stairwell in an office building using phaseless 28 GHz robotic measurement scans. The calibration constrains the geometric and material parameters to realistic ranges and uses only training measurements. Separate *held-out* planes test the selected model. The calibrated digital twin reproduces the broad spatial distribution and the strongest interference spacings on every held-out plane. We then use its complex field for in-situ dosimetry on an anatomical phantom walking through the room. For a milliwatt-class source, the peak whole-body specific absorption rate is 6.7×10^{-8} W/kg and the peak absorbed power density over 4 cm^2 is 1.5×10^{-5} W/m^2. These results show that phaseless scans can validate a digital twin for indoor exposure assessment.**

***Index Terms*—Digital twin, 28 GHz, phaseless calibration, blind validation, indoor exposure, absorbed power density, ray tracing**

I. Introduction

Absorbed power density (APD) is an important dosimetric quantity above 6 GHz under the 2020 International Commission on Non-Ionizing Radiation Protection (ICNIRP) guidelines [1]. Indoor compliance assessment needs spatial field distributions. Single-point measurements and free-space calculations cannot provide them [2], [3]. Robotic scanning with a calibrated electric-field probe at millimeter-wave (mmWave) frequencies can produce accurate phaseless amplitude maps [4]. The method is slow (31 hours for five planar slices of an $85 \times 40 \times 70$ cm domain at 28 GHz [4]) and covers only the scanned positions. The fields between and beyond the measured planes, and the absorption on a person in the room, cannot be obtained from the scan alone.

Ray tracing predicts indoor mmWave fields from geometry and material properties [5], [6]. Material parameters at 28 GHz are available from standards [7] and channel measurements [8]. Hybrid approaches combine simulated and measured fields for exposure assessment [9], [10]. Equivalent-current methods reconstruct sources from near-field scans and compute power density [11]. However, both approaches need a simulation or reconstruction that measurements verify.

No existing method has shown that a simulation with physical parameters can reproduce phaseless mmWave measurements in a real indoor environment. Without validation, the accuracy of digital-twin exposure estimates is unknown. A model with many free parameters can fit measurement artifacts instead of physical structure. Agreement on training measurements alone does not show that the model will reproduce unseen measurements.

This letter makes three contributions. First, we calibrate a digital twin of a real indoor environment using phaseless 28 GHz scans. The calibration varies about ten geometric parameters, including the antenna pose and scan-frame alignment, together with the material properties. Each measurement plane is held out in turn, while only the remaining planes select the model. The digital twin reproduces the main spatial power distribution and strongest interference spacings on the held-out planes. Second, the magnitude data identify the direction of the largest missing arrival and associate it with a periodic metal railing. Third, we use the calibrated digital twin for real in-situ surface absorbed power dosimetry. We compute whole-body specific absorption rate ($\mathrm{SAR_{wb}}$) and peak absorbed power density averaged over 4 cm^2 ($\mathrm{APD_{4\,cm^2}}$) for a person walking through the room, including the CENELEC three-height body average. Section II describes the measurement configuration, calibration method, and exposure computation. Section III presents the blind validation and exposure results.

Fig. 1 shows the configuration used for the measurement and exposure assessment.

II. Methods

A. Configuration

Figs. 1a and 1b show the measurement and its digital twin. The stairwell has concrete walls and a metal railing. It is a realistic indoor environment without significant clutter. The transmitter is a four-element 28 GHz phased array fed through a Butler matrix [12], with port 3 driven [13]. A three-axis robot with sub-mm positioning carries a calibrated Narda uniaxial electric-field probe (26.5–29.5 GHz) [14] through five planes of an $85 \times 40 \times 70$ cm volume at $\lambda/4$ resolution [4]. The probe

Manuscript received MONTH DAY, YEAR; revised MONTH DAY, YEAR. This work was supported by TODO. (Corresponding author: Robin Wydaeghe.)

The authors are with the WAVES research group, Department of Information Technology, Ghent University–imec, Technologiepark-Zwijnaarde 126, 9052 Ghent, Belgium (e-mail: robin.wydaeghe@ugent.be).

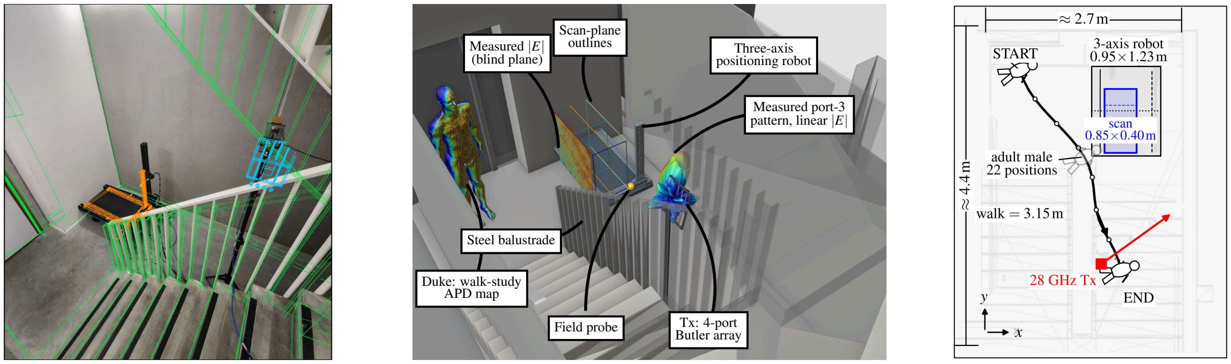

(a) Photograph and digital-twin overlay.

(b) Digital twin, antenna pattern, measured plane, and phantom.

(c) Top view of the 3.2 m walk.

Fig. 1. Configuration of the 28 GHz measurement and its digital twin. (a) The three-axis robot scans five planes in the stairwell. (b) The digital twin contains the measured antenna pattern, room geometry, measurement plane, and Duke phantom. (c) The adult male phantom walks 3.2 m through 22 positions from the marked start to end, past the robot and scan volume toward the transmitter.

axis and the modeled field component are aligned with the room's y-direction. The five scans took 31 hours. One plane (x=40 cm) is excluded from all scores because its repeatability at the intersection of two scans is low ($r \leq 0.32$, versus ≈ 0.9 for the other planes). The scans contain a multiplicative instrument response and a timing offset that depends on scan direction. Both are corrected before comparison [4].

The room geometry comes from an accurate architectural model. Material classes (concrete, masonry, plaster) have electromagnetic parameters constrained to standard ranges [7]. The antenna radiation pattern is obtained from an anechoic-chamber measurement [13]. Movable equipment is not modeled. The stair railing is present in the traced scene as flat metal, but its grating-like diffraction falls outside specular ray tracing.

B. Calibration

The power delivered to the antenna is not measured directly because losses in the source chain are unknown. The comparison metrics are scale-invariant. For exposure, the simulated field is scaled to the absolute probe amplitude on the training planes. The digital twin has approximately ten continuous pose parameters (antenna position and orientation, scan-frame alignment, probe offset, pattern roll) and eight material parameters (permittivity and conductivity for each of four wall classes). All parameters are constrained to physically realistic ranges [7]. The ray tracer uses single-bounce specular paths.

Three comparison metrics test different spatial scales. First, we correlate the measured and predicted field magnitude after Gaussian smoothing with a standard deviation of 2λ. This metric measures the broad spatial power distribution. Second, we define the *beat spectrum* as the mean magnitude spectrum of the scan rows within the physical interference band from 0.35 to 2.05 cycles per wavelength. It measures interference spacing and is unchanged by a spatial shift. Third, raw Pearson correlation measures point-by-point agreement. The parameter search uses the smoothed-field correlation because raw correlation has a local optimum at every $\lambda/4$ of position error. The final selection uses the beat spectrum to test interference structure without requiring exact spatial alignment.

Table I lists the four held-out planes and their scores. The model is ranked on training planes only. Ranking on held-out planes produced candidates with negative training correlation, which is data leakage. The held-out data test the selection but never select the model. This separation gives blind validation. Each of the four remaining measurement planes is held out in turn. The selected candidate maximizes the sum of the smoothed-field and beat-spectrum correlations on the training planes. In a synthetic test with known ground truth, the same procedure ranked the correct answer first among 41 candidates [4].

C. Exposure Computation

Fig. 1c shows a top view of the realistic walking scenario. An adult male walks 3.2 m through the field of the 28 GHz transmitter. The calibrated digital twin provides the full complex field over this walk. At 28 GHz, the skin depth is a fraction of a millimeter [15], so absorption occurs near the body surface. At each walk position, the ray tracer samples the incident field on a Huygens box around the anatomical phantom. Love's equivalence principle transfers this field to the body surface [16]. Fresnel transmission and directional self-shadowing then give $\mathrm{SAR}_{\mathrm{wb}}$ and $\mathrm{APD}_{4\,\mathrm{cm}^2}$ on the posed Duke phantom [17]. The 4 cm^2 averaging area is the ICNIRP 2020 basic restriction for local exposure from 6 to 300 GHz. We also report APD over 1 cm^2 as an informative quantity. The 1 cm^2 criterion applies above 30 GHz, where its limit is twice the 4 cm^2 value. Following the CENELEC in-situ protocol, we also form a body-representing vertical average from incident power-density samples at 1.1, 1.5, and 1.7 m above the floor [18], [19].

III. Results

A. Validation

Fig. 2 shows the validation on the held-out y=40 cm plane.

Table I lists the blind validation scores on all four held-out planes. The beat-spectrum correlation ranges from +0.55 to

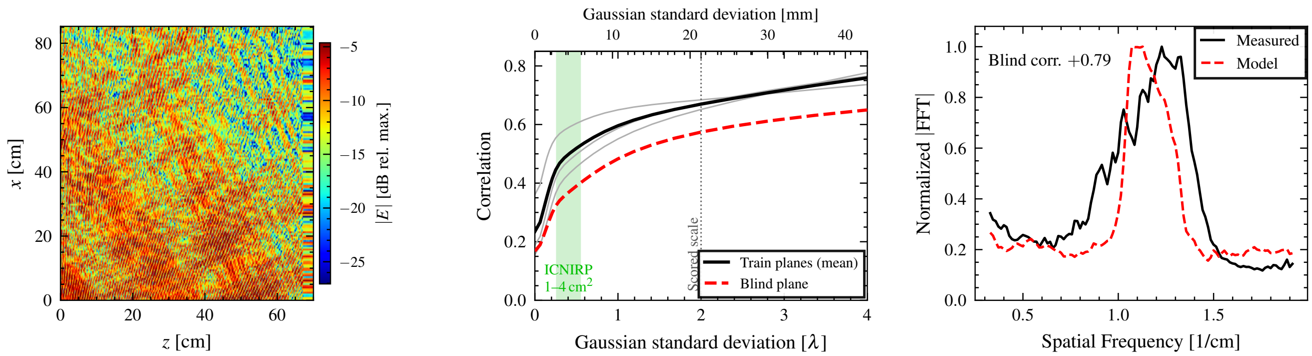

(a) Measured $|E|$ on the held-out plane. (b) Correlation after Gaussian smoothing. (c) Normalized beat spectrum.

Fig. 2. Blind validation on the held-out y=40 cm plane. (a) Measured field magnitude in dB, normalized to its maximum. (b) Pearson correlation after Gaussian smoothing. Black is the mean of the training planes and red is the held-out plane. (c) Measured and predicted beat spectra, each normalized to its maximum.

TABLE I
VALIDATION ON MEASUREMENT PLANES HELD OUT IN TURN. PEARSON CORRELATIONS COMPARE MODEL AND MEASUREMENT ON EACH HELD-OUT PLANE. THE SMOOTHED-FIELD METRIC USES A GAUSSIAN STANDARD DEVIATION OF 2λ.

Held-out plane	Smoothed $\|E\|$	Beat spectrum	Raw
x=0	+0.19	+0.57	+0.08
y=0	+0.53	+0.55	+0.13
y=20 cm	+0.67	+0.75	+0.20
y=40 cm	+0.56	+0.79	+0.17
Mean	+0.49	+0.66	+0.15

+0.79, smoothed-field correlation from +0.19 to +0.67 (mean +0.49), and raw correlation is positive on every held-out plane. The agreement grows monotonically with smoothing, so the smoothed-field correlation can be made as high as desired if the smoothing scale is not fixed. The Gaussian standard deviation is fixed at 2λ for these scores.

Fig. 2b shows how averaging affects the correlation. The value for the held-out plane rises from +0.17 without smoothing to +0.57 at the scored scale (2λ) and +0.65 at 4λ. The training-plane mean follows the same trend at higher values. The green band marks the ICNIRP 1–4 cm^2 averaging apertures. Fig. 2c shows that the strongest interference spacings are well predicted: the beat spectrum of the held-out plane has a correlation of +0.79. The measured field has two to three times as much fine-scale variation as the model, consistent with interference from non-specular paths that the model does not include.

Adding second-bounce specular paths and diffuse scattering both increase the smoothed-field correlation but reduce the beat-spectrum agreement to near zero. Material parameters close to a perfect electric conductor (PEC) produce the opposite result: the beat-spectrum agreement increases, but the smoothed-field agreement decreases. A smoothed-field metric alone cannot separate agreement in the broad power distribution from agreement in the interference pattern. Therefore, the search uses the smoothed field and the selection uses the beat spectrum. These tests show that the held-out beat-spectrum correlations in Table I measure interference agreement.

On every scan plane, the two-dimensional beat spectrum isolates one measured interference pair absent from the model. A two-ray arrival model places the missing scatterer at elevation $+26°$ to $+30°$, azimuth $\approx \pm 95°$ from the antenna boresight. This direction points to the stair railing (Fig. 1c), a periodic metal grating with pitch $\approx 9.3\lambda$. The grating cannot be modeled by specular ray tracing and is the digital twin's main known limitation. Confirming this attribution requires wave-capable modeling of the grating or a controlled absorber measurement.

B. Exposure

Fig. 3 shows the exposure along the realistic walk in Fig. 1c. We use the digital twin selected without the y=40 cm plane (Table I). The 3.2 m path runs from the marked start, past the scan volume, to within 0.47 m of the antenna. At each of 22 positions, the ray tracer exports the complex electric-field Jones vectors on the Huygens box. The source-chain losses were not measured, so the power delivered to the antenna is unknown. The exposure calculation instead uses the absolute field magnitude measured by the probe. This is a milliwatt-class source.

The peak $\mathrm{APD}_{4\,\mathrm{cm}^2}$ is 1.5×10^{-5} W/m^2 and the peak $\mathrm{SAR}_{\mathrm{wb}}$ is 6.7×10^{-8} W/kg, both over 60 dB below the ICNIRP 2020 general-public basic restrictions (20 W/m^2 and 0.08 W/kg, respectively). The peak $\mathrm{APD}_{1\,\mathrm{cm}^2}$ is 1.5×10^{-5} W/m^2. Its ratio to the 4 cm^2 value is 1.01, which shows that the incident field is smooth at centimeter scale on the body surface, consistent with the scan-plane result in Fig. 2b. The three-height average peaks at 4.2×10^{-4} W/m^2, which is 44 dB below the 10 W/m^2 whole-body incident-power-density reference level. Exposure is maximized near the antenna, where direct and reflected paths add. Both quantities drop by two to three orders of magnitude in the scanner shadow, where the direct path is blocked. The exposure values scale linearly with radiated power.

On the held-out y=40 cm plane, the model under-predicts local power by a median of 1.9 dB (−0.8 to +4.9 dB, 5th–95th percentile). We recompute the exposure walk with each of the four selected models, one for each held-out plane. The peak

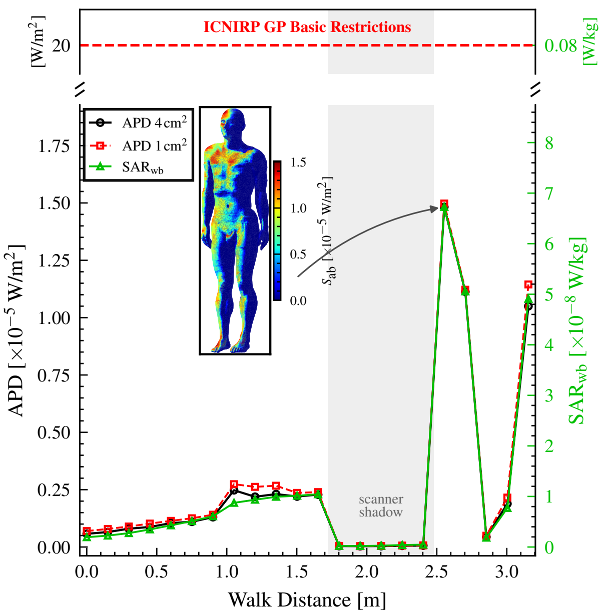

Fig. 3. Exposure along the 3.2 m walk for a milliwatt-class source. The left axis gives $\mathrm{APD}_{4\,\mathrm{cm}^2}$ and $\mathrm{APD}_{1\,\mathrm{cm}^2}$. The right axis gives $\mathrm{SAR}_{\mathrm{wb}}$. Dashed lines above the break mark the ICNIRP 2020 general-public basic restrictions. The inset shows surface S_{ab} at the maximum.

$\mathrm{APD}_{4\,\mathrm{cm}^2}$ spans 7 dB across these models, from 1.5×10^{-5} to 7.6×10^{-5} W/m^2. The worst-case model is still 54 dB below the general-public basic restriction. Both the local-power error (≤ 5 dB) and the parameter spread ($\sim$7 dB) are small compared to this margin.

IV. Conclusion

We calibrated a ray-tracing digital twin of a real indoor room on phaseless 28 GHz scans and validated it with blind held-out planes. The digital twin predicts the held-out interference beat spectra with Pearson correlation $+0.55$ to $+0.79$ across four held-out planes. The magnitude data also identify the direction of the largest missing arrival. The digital twin, combined with Huygens-box surface dosimetry, gives $\mathrm{SAR}_{\mathrm{wb}}$ and $\mathrm{APD}_{4\,\mathrm{cm}^2}$ for a person walking through the room. For a milliwatt-class source, both quantities remain over 54 dB below the general-public basic restrictions.

This work shows that phaseless scans can validate a digital twin for indoor exposure computation at 28 GHz when separate measurements select and test the model. The main limitation is the specular ray model, which cannot represent the periodic railing. Future work will consist of wave-capable modeling of such structures and tests in larger environments.

Acknowledgment

References

[1] ICNIRP, "Guidelines for limiting exposure to electromagnetic fields (100 kHz to 300 GHz)," *Health Phys.*, vol. 118, no. 5, pp. 483–524, May 2020.

[2] B. Thors, D. Colombi, Z. Ying, T. Bolin, and C. Tornevik, "Exposure to RF EMF from array antennas in 5G mobile communication equipment," *IEEE Access*, vol. 4, pp. 7469–7478, 2016.

[3] D. Colombi, B. Thors, and C. Tornevik, "Implications of EMF exposure limits on output power levels for 5G devices above 6 GHz," *IEEE Antennas Wireless Propag. Lett.*, vol. 14, pp. 1247–1249, 2015.

[4] R. Wydaeghe *et al.*, "Holographic phase retrieval of RF-EMFs for human exposure assessment using fine 3D electric field measurements in a real environment from a beamforming 28 GHz antenna," in *Proc. Eur. Conf. Antennas Propag. (EuCAP)*, Stockholm, Sweden, Mar.–Apr. 2025, pp. 1–5.

[5] J. Hoydis *et al.*, "Sionna RT: Differentiable ray tracing for radio propagation modeling," in *Proc. IEEE Globecom Workshops*, 2023, pp. 317–321.

[6] V. Degli-Esposti, F. Fuschini, E. M. Vitucci, and G. Falciasecca, "Measurement and modeling of scattering from buildings," *IEEE Trans. Antennas Propag.*, vol. 55, no. 1, pp. 143–153, Jan. 2007.

[7] ITU-R, "Effects of building materials and structures on radio-wave propagation in the range of 1 MHz to 450 GHz," Rec. ITU-R P.2040-4, Sep. 2025.

[8] J. Hoydis *et al.*, "Learning radio environments by differentiable ray tracing," *IEEE Trans. Mach. Learn. Commun. Netw.*, vol. 2, pp. 1527–1539, 2024.

[9] R. Wydaeghe *et al.*, "Hybrid ray-tracing-QuaDRiGa/FDTD method for realistic 28 GHz exposure with 6G CF-MaMIMO in 3D outdoor environments," *npj Wireless Technol.*, vol. 2, art. 13, 2026.

[10] D. Colombi *et al.*, "Analysis of the actual power and EMF exposure from base stations in a commercial 5G network," *Appl. Sci.*, vol. 10, no. 15, p. 5280, 2020.

[11] W. He *et al.*, "Fast power density assessment of 5G mobile handset using equivalent currents method," *IEEE Trans. Antennas Propag.*, vol. 69, no. 10, pp. 6857–6869, Oct. 2021.

[12] L. Van Messem *et al.*, "A 4×4 millimeter-wave-frequency Butler matrix in grounded co-planar waveguide technology for compact integration with 5G antenna arrays," *IEEE Trans. Microw. Theory Techn.*, vol. 71, no. 1, pp. 122–134, Jan. 2023.

[13] I. L. de Paula *et al.*, "Cost-effective high-performance air-filled SIW antenna array for the global 5G 26 GHz and 28 GHz bands," *IEEE Antennas Wireless Propag. Lett.*, vol. 20, no. 2, pp. 194–198, Feb. 2021.

[14] Narda Safety Test Solutions, "Measurement of 5G NR FR2 electromagnetic fields," Pfullingen, Germany, Rep. NSTS 0922-E0377B.

[15] S. Gabriel, R. W. Lau, and C. Gabriel, "The dielectric properties of biological tissues: III. Parametric models for the dielectric spectrum of tissues," *Phys. Med. Biol.*, vol. 41, no. 11, pp. 2271–2293, Nov. 1996.

[16] J. D. Jackson, *Classical Electrodynamics*, 3rd ed. New York, NY, USA: Wiley, 1998.

[17] A. Christ *et al.*, "The Virtual Family—Development of surface-based anatomical models of two adults and two children for dosimetric simulations," *Phys. Med. Biol.*, vol. 55, no. 2, pp. N23–N38, Jan. 2010.

[18] CENELEC, "Basic standard for the in-situ measurement of electromagnetic field strength related to human exposure in the vicinity of base stations," EN 50492:2008, Nov. 2008.

[19] IEC, "Determination of RF field strength, power density and SAR in the vicinity of base stations for the purpose of evaluating human exposure," IEC 62232:2025, Apr. 2025.